Contents lists available at ScienceDirect

Minerals Engineering

journal homepage: www.elsevier.com/locate/mineng

Particle–bubble interaction energies for particles with physical and chemical heterogeneities

Allan Gomez-Flores[a], Scott A. Bradford[b], Gukhwa Hwang[a], Graeme W. Heyes[c], Hyunjung Kim[a,*]

[a] Department of Mineral Resources and Energy Engineering, Jeonbuk National University, 567, Baekje-daero, Deokjin-gu, Jeonju, Jeonbuk 54896, Republic of Korea
[b] US Salinity Laboratory, USDA, ARS, Riverside, CA, USA
[c] CSIRO, Mineral Resources Division, Clayton, Victoria 3169, Australia

ARTICLE INFO

Keywords:
Flotation
XDLVO
Surface roughness
Charge heterogeneity
Contact angle heterogeneity

ABSTRACT

The interaction between a particle and bubble in a liquid medium is important in processes such as mineral flotation or paper deinking. The sum of van der Waals, electrostatic, and hydrophobic interaction energies can be calculated to predict if the net interaction is favorable or unfavorable for the particle to attach to the bubble. However, conventional interaction energy calculations only relate to smooth and chemically homogeneous surfaces. Particles used in flotation have natural and induced heterogeneities such as surface roughness (SR), surface charge heterogeneity (CH), and surface contact angle heterogeneity (CAH). We therefore numerically investigated the bubble – particle interaction energy for seven hypothetical combinations of SR, CH and CAH on the particle. It was found that the strength in which the heterogeneities influence the interaction energy barrier is in the order of CAH < SR < CH. The present work is the first to provide a full theoretical view of how heterogeneities individually and in combination influence particle – bubble interactions.

1. Introduction

Interactions between particles and surfaces are important in various science fields and applications such as for example: colloid transport and retention in porous media (Cai et al., 2015; Han et al., 2016; Peng et al., 2017), flotation (Choi et al., 2016; Kim et al., 2017; Park et al., 2015), drug delivery (Falconer and Grainger, 2018; Gupta and Gupta, 2005), or bioleaching (Silva et al., 2015a; Silva et al., 2015b). The interactions can result in attachment of particles on a surface, and this surface can be a solid or gas phase. Specifically, flotation is a representative process of particle attachment to a gas phase (bubble surface).

The Derjaguin, Landau, Verwey, and Overbeek (DLVO) theory is used to calculate interaction energies that physicochemically interpret the attachment of particles onto a surface and can predict whether it will or will not occur. Classically, the DLVO theory consists of the sum between the van de Waals (VDW) and the electric double layer (EDL) interactions. The presence or absence of an energy barrier (Φ_{max}) indicates whether conditions are unfavorable or favorable for the attachment, respectively. The classic DLVO theory has been useful in describing the attachment that occurs in solid–liquid–solid systems. However, it fails to describe the attachment when occurs in modern mineral flotation due to the presence of a gas phase, non–polar materials, and acid–base interactions (Israelachvili and Pashley, 1984; Vanoss, 1993). In this case, the classic DLVO theory has to be extended by including the hydrophobic (HYPB) interaction (Yoon and Mao, 1996) and the summation of the three interactions is called the extended DLVO (XDLVO) theory.

In this study we investigate the attachment of a hydrophobic particle to an air bubble in water (flotation). From Dr. J. A. Kitchener in the 1950's the DLVO theory has been related to flotation (Ralston, 2020), his legacy remains and it is our desire to contribute. The classical DLVO and XDLVO theories assumed that interactions occurred between physically and chemically homogeneous surfaces. However, in reality both physical (shape or surface imperfections) and chemical (charge or hydrophobicity) heterogeneities are present on surfaces of mineral particles (Gaudin, 1932). Uneven surfaces having ridges and craters are called surface roughness. Roughness may occur due to chemical pretreatments, grinding, comminution processes (Ahmed, 2010; Hassas et al., 2016), or microorganism activity (Han et al., 2016). For practical representations, surface roughness can be thought as pillars of certain height distributed on a surface. Different charges on a surface are called charge heterogeneity. Charge heterogeneities can occur due to natural variation of functional groups on a surface, naturally embedded materials of different composition (impurities), uneven collector adsorption on a natural surface or liberated minerals, or due to any chemical

* Corresponding author.
E-mail address: kshjkim@jbnu.ac.kr (H. Kim).

https://doi.org/10.1016/j.mineng.2020.106472
Received 24 March 2020; Received in revised form 16 May 2020; Accepted 17 May 2020

Nomenclature

A_{132}	Combined Hamaker constant of particle (1) and bubble (2) interacting in water (3)
A_{11}	Hamaker constant of particle
A_{22}	Hamaker constant of air
A_{33}	Hamaker constant of water
b	Parameter characterizing materials of interaction particles
c	Speed of light
CH	Surface charge heterogeneity
CAH	Contact angle heterogeneity
d_b	Bubble diameter
d_p	Particle diameter
E_k	Kinetic energy of particle
ε_0	Permittivity on a vacuum
ε_3	Dielectric constant of water
EDL	Electric double layer interaction
f_{Low}	Fraction of low contact angle
f_{p+}	Fraction of positive charge
f_{SR}	Fraction of surface roughness
H	Separation distance
h_{SR}	Height of surface roughness
HYPB	Hydrophobic interaction
κ	Debye–Hückel parameter
K_{132}	Hydrophobic force constant of the particle–bubble-water system
l	Constant for the water
m_p	Mass of particle
IS	Ionic strength
$\Phi_{2\min}$	Secondary minima
Φ_{EDL}	EDL interaction for homogeneous surfaces
$\Phi_{EDL,het}$	EDL interaction having SR and/or CH
Φ_{HYPB}	HYPB interaction for homogeneous surfaces
$\Phi_{HYPB,het}$	HYPB interaction having SR and/or CAH
$\Phi_{\max}$	Energy barrier
$\Phi_{T,het}$	Total interaction energy of a physically and chemically heterogeneous particle surface
Φ_{VDW}	Retarded VDW interaction of a homogeneous surface
$\Phi_{VDW,het}$	Retarded VDW interaction having SR
SR	Surface roughness
θ	Relatively hydrophobic contact angle
θ_{Low}	Low contact angle
VDW	van der Waals interaction energy
vel_p	Particle velocity at critical distance
ξ_b	Zeta potential of bubble
ξ_{p-}	Negative zeta potential of particle
ξ_{p+}	Positive zeta potential of particle

change or pretreatment before a subsequent process during mineral processing (e.g., surface oxidation due to grinding) (Drelich and Wang, 2011; Gaudin, 1932; Kulkarni and Somasundaran, 1976; Song and Elimelech, 1994; Zhang et al., 2016). Charge heterogeneity can be thought as a grid on a surface where the squares have random positive or negative charge. Similarly, different degrees of hydrophobicity (hydrophilicity) represented by a contact angle on a surface are called contact angle heterogeneity. Contact angle heterogeneities can occur due to uneven collector adsorption caused by surface roughness and charge heterogeneity, liberation or surface oxidation during grinding, chemical treatments during mineral processing, or surface composition (Drelich and Wang, 2011; Gaudin, 1932; Kulkarni and Somasundaran, 1976; Medout-Marere et al., 2000; Xie et al., 2017). Contact angle heterogeneity can be thought as a grid on a surface where the squares have different contact angles.

The effect of surface roughness on particle–bubble interactions has been experimentally and theoretically investigated by a limited number of studies concerning flotation (Chen et al., 2018; Drelich, 2018; Drelich and Bowen, 2015; Guven and Celik, 2016; Guven et al., 2015; Guven et al., 2016; Hassas et al., 2016; Nikolaev, 2016; Xia, 2017; Xing et al., 2017; Yin et al., 2018). Experimentally, it has been reported that particle roughness generally increased flotation rate constants, reduced the nano time of water film thining and rupture between a particle and a bubble, improved particle attachment, increased the flotation

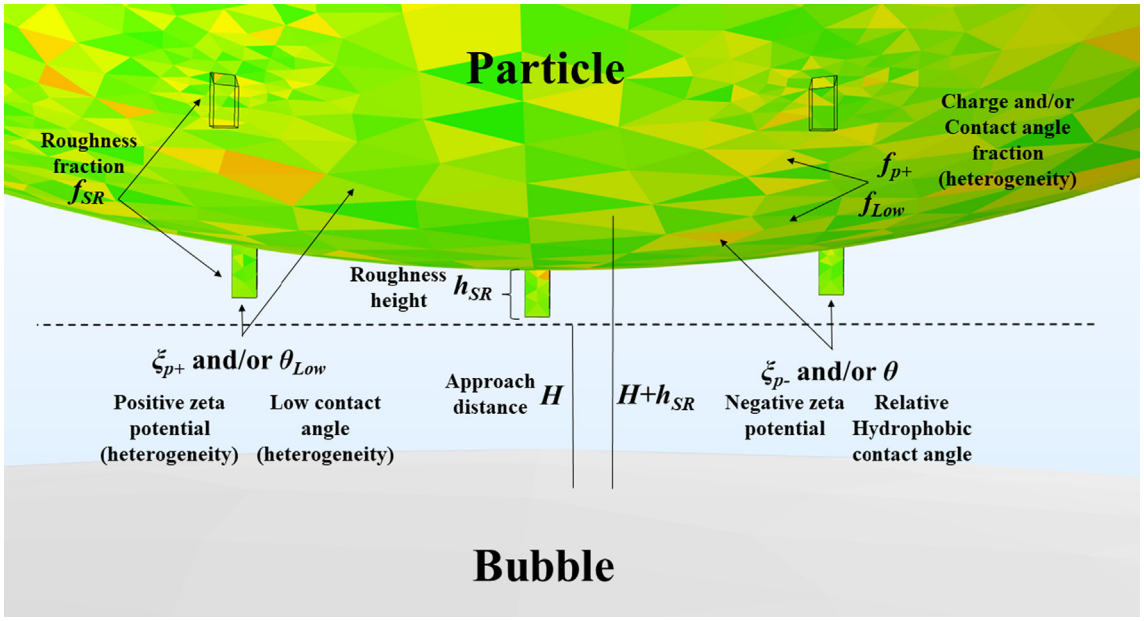

Fig. 1. Schematic representation of the SR, CH, and CAH on the particle within the zone of influence. Here h_{SR} is the height of the roughness on the colloid, H is the separation distance from h_{SR} to the bubble. The different colors on the particle represent positive zeta potential (ξ_{p+}), negative zeta potential (ξ_{p-}), hydrophobic contact angle (θ), and/or low contact angle (θ_{Low}).

recovery, and increased the contact angle. Theoretically, it has been reported that particle sub–microscopic roughness reduced the Φ_{max} significantly. Only a few tens of nanometers are sufficient to greatly decrease Φ_{max} and produce favorable conditions for attachment. Particle–bubble interactions that considered surface roughness has been successfully related to experimental observations of flotation of rough glass particles (Drelich and Bowen, 2015). Conversely, the role of chemical (charge or hydrophobicity) heterogeneities or the combined (synergy) role of surface roughness and chemical heterogeneity on particle–bubble interaction has not yet been reported. The study of individual and combined heterogeneities on particle–bubble interactions is needed to clearly identify controlling mechanisms and to optimize the design of mineral flotation.

In this study we conduct a systematic theoretical investigation of the effect of particle physical (roughness) and chemical (charge and contact angle) heterogeneities on particle–bubble interactions. The effect of each heterogeneity is investigated individually and in combinations, resulting in a total of seven cases of heterogeneity.

2. Materials and methods

In this study, we assume that a spherical methylated glass particle interacts with an air bubble in a monovalent electrolyte solution of a given ionic strength (IS). Only the particle exhibits surface roughness (SR), charge heterogeneity (CH) and contact angle heterogeneity (CAH). The approach to calculate the interaction energies using the XDLVO theory considering surface heterogeneities is based on previous literature (Bradford et al., 2017; Bradford et al., 2018), where the XDLVO theory is calculated as a linear summation of interaction energies associated with combinations of fractions of SR, CH, and CAH. Fig. 1 presents a schematic illustrating SR, CH and CAH on the particle during interaction with a bubble. The particle exhibits fractions of surface heterogeneities within an area of electrostatic zone of influence. The zone of electrostatic influence is proportional to the colloid radius and the Debye length. The fractions are equally distributed, do not overlap, and represent a percentage of area. The particle contains a SR fraction (f_{SR}) with a height equal to h_{SR}, a positive charge fraction (f_{p+}) equal to a positive zeta potential ξ_{p+}, and a low contact angle fraction (f_{Low}) represented with a contact angle θ_{Low}. The complementary fractions ($1–f_{SR}$), ($1-f_{p+}$), and ($1-f_{Low}$) correspond to a smooth surface, a negative zeta potential ξ_{p-}, and a relatively hydrophobic contact angle θ, *respectively*. The equation of the XDVLO interaction energy having ternary heterogeneity is defined as

$$\Phi_{T,het}(H) = \Phi_{VDW,het} + \Phi_{EDL,het} + \Phi_{HYPB,het} \quad (1)$$

where H is the separation distance from the bubble surface to the leading face of the particle center at a height h_{SR} (see Fig. 1), $\Phi_{T,het}$ is the total interaction energy of a physically and chemically heterogeneous surface. The retarded VDW interaction with SR contributions ($\Phi_{VDW,het}$), the EDL interaction with SR and/or CH contributions ($\Phi_{EDL,het}$), and the HYPB interaction with SR and/or CAH contributions ($\Phi_{HYPB,het}$) were the considered, and are defined as

$$\Phi_{VDW,het} = (1-f_{SR})\Phi_{VDW}(H+h_{SR}) + f_{SR}\Phi_{VDW}(H) \quad (2)$$

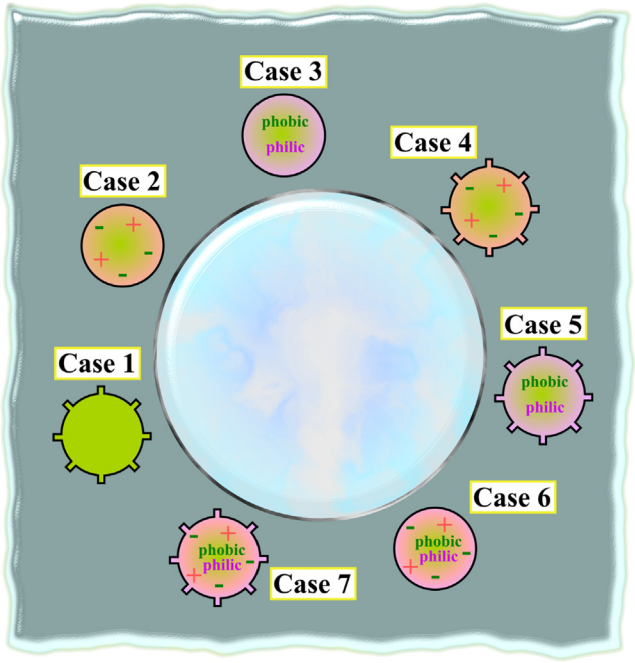

Fig. 2. Cartoon illustrating the seven cases of particle heterogeneity. Case 1: only SR; case 2: only CH; case 3: only CAH; case 4: SR and CH; case 5: SR and CAH; case 6: CH and CAH; case 7: SR, CH, and CAH. More details on heterogeneity fractions and other parameters can be seen in Table 1. The sizes and heterogeneity distributions in this figure are not in real scale.

$$\Phi_{EDL,het} = (1-f_{SR})(1-f_{p+})\Phi_{EDL}(H+h_{SR},\xi_{p-}) + (1-f_{SR})f_{p+}\Phi_{EDL}(H+h_{SR},\xi_{p+}) + f_{SR}f_{p+}\Phi_{EDL}(H,\xi_{p+}) + f_{SR}(1-f_{p+})\Phi_{EDL}(H,\xi_{p-}) \quad (3)$$

$$\Phi_{HYPB,het} = (1-f_{SR})(1-f_{Low})\Phi_{HYPB}(H+h_{SR},\theta) + (1-f_{SR})f_{Low}\Phi_{HYPB}(H+h_{SR},\theta_{Low}) + f_{SR}f_{Low}\Phi_{HYPB}(H,\theta_{Low}) + f_{SR}(1-f_{Low})\Phi_{HYPB}(H,\theta) \quad (4)$$

where Φ_{VDW} is the VDW interaction energy for homogeneous surfaces, Φ_{EDL} is the EDL interaction energy for homogeneous surfaces, Φ_{HYPB} is the HYPB interaction energy for homogeneous surfaces.

The VDW (Yoon and Mao, 1996), EDL (constant surface potential) (Hogg et al., 1966), and HYPB (Van Oss, 1994) interaction energies for homogeneous surfaces are defined respectively as

$$\Phi_{VDW} = -\frac{A_{132}}{6H}\frac{d_p d_b}{2(d_p+d_b)}\left[1-\frac{1+2bl}{1+bc/H}\right]$$
$$\Phi_{EDL} = \pi\varepsilon_0\varepsilon_3\frac{d_p d_b}{2(d_p+d_b)}\left\{2\xi_p\xi_b\ln\left[\frac{1+\exp(-\kappa H)}{1-\exp(-\kappa H)}\right] + (\xi_p^2+\xi_b^2)\ln[1-\exp(-2\kappa H)]\right\}$$
$$\Phi_{HYPB} = -\frac{K_{132}}{H}\frac{d_p d_b}{2(d_p+d_b)} \quad (5)$$

Table 1
Summary of SR, CA, CAH, and experimental parameters for the numerical experiments.

Case	Figure	d_p (μm)	h_{SR} (nm)	f_{SR} (-)	ξ_{p+} (mV)	f_{p+} (-)	θ (deg)	θ_{Low} (deg)	f_{Low} (-)
1: only SR	3	20, 120	0–1000	0–1	0	0	35	0	0
2: only CH	4	20, 120	0	0	0–60.7	0–1	35	0	0
3: only CAH	5	20	0	0	0	0	35, 64	5	0–1
4: SR and CH	6	120	10, 100	0–1	12.2, 36.5	0–1	35	0	0
5: SR and CAH	7	120	10, 100	0–1	0	0	35	5, 20	0–1
6: CH and CAH	8	120	0	0	12.2, 36.5	0–1	35	5, 20	0–1
7: SR, CA and CAH	9, 10	120	10, 100	0–1	6.1, 30.4	0–1	35, 75	5, 20	0–1

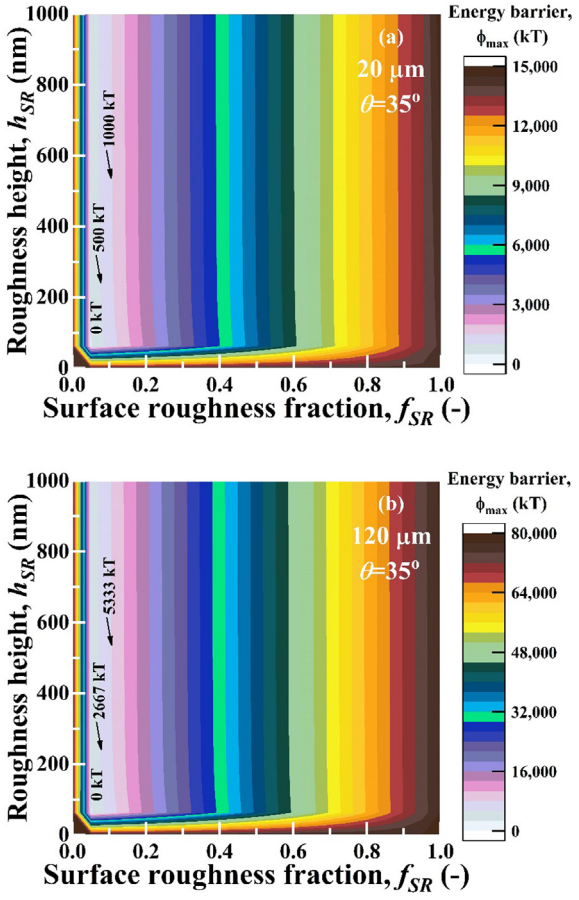

Fig. 3. Case 1: Contour plots of the XDLVO energy barrier for particle–bubble interaction as a function of h_{SR} and its fraction for d_p = (a) 20 and (b) 120 μm. Other conditions are d_b = 1 mm, ξ_p = −60.75 mV, ξ_b = −32.78 mV, IS = 1 mM, κ^{-1} = 9.63 nm. Note the difference in scale.

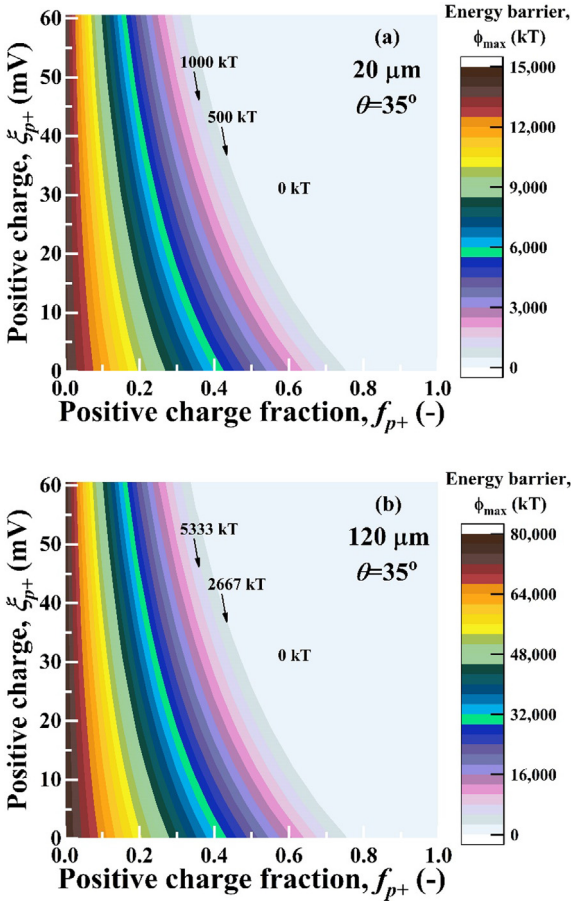

Fig. 4. Case 2: Contour plots of the XDLVO energy barrier for particle–bubble interaction as a function of ξ_{p+} and its fraction for d_p = (a) 20 and (b) 120 μm. Other conditions are d_b = 1 mm, ξ_p = −60.75 mV, ξ_b = −32.78 mV, IS = 1 mM, κ^{-1} = 9.63 nm. Note the difference in scale.

where A_{132} (J) is the combined Hamaker constant of particle 1 and bubble 2 interacting in water 3, b is a parameter characterizing materials of interaction particles which was set to 3×10^{-17} s (Yoon and Mao, 1996), l is a constant for the medium (water) of 3.3×10^{15} s^{-1} (Yoon and Mao, 1996), c (m/s) is the speed of light, ε_0 (F/m) is the permittivity on a vacuum, ε_3 (−) is the dielectric constant of water, d_p (m) is the particle diameter, d_b (m) is the bubble diameter of 1 mm (average size in flotation cells) (Koh and Schwarz, 2006), ξ_{p-} (V) is the zeta potential of the particle of −60.75 mV at an IS of 1 mM (Yoon and Mao, 1996), ξ_b (V) is the zeta potential of the bubble of −32.78 mV at 1 mM IS (Yoon and Mao, 1996), κ (1/m) is the Debye–Hückel parameter, and K_{132} (J) is the hydrophobic force constant of the particle–bubble-water system which was related to the water contact angle of methylated glass spheres by fitting previously reported data (Yoon and Mao, 1996). Since the Hamaker constant for water (A_{33} = 3.7×10^{-20} J) (Israelachvili, 2011) is less than those of silica/glass particles (A_{11} = 6.5×10^{-20} J) (Israelachvili, 2011) but is greater than that of air (A_{22} = 0 J) (Israelachvili, 2011), A_{132} is usually negative. Thus, the VDW interaction between bubble and particle is repulsive. Finally, A_{132} (Israelachvili, 2011) and K_{132} were respectively calculated as

$$A_{132} = (\sqrt{A_{11}} - \sqrt{A_{33}})(\sqrt{A_{22}} - \sqrt{A_{33}}) \quad (6)$$

$$K_{132} = 6x10^{-21}\exp(0.0623\theta) \quad (7)$$

Particle–bubble interaction can be divided in three steps which are collision, attachment, and detachment (Koh and Schwarz, 2006; Yoon and Mao, 1996). Other physics underlying the attachment and detachment on particle–bubble aggregates in agitated tanks include the gravity force, buoyancy force, capillary force, and turbulence (Koh and Schwarz, 2006; Yoon and Mao, 1996). Nevertheless, attachment and the VDW, EDL and HYPB interactions are our focus in this study. Note that Born repulsion is sometimes included in the XDLVO calculations that consider detachment (Bradford et al., 2018), but was neglected in this study because attractive capillary force dominates after attachment when particles enter the bubble.

A sphere–sphere configuration for the interaction energies and numerical experimental parameters (range of roughness height, zeta potential, particle diameters, bubble diameter, contact angle, and others in the set of equations) were selected based on previous literature (Chen et al., 2018; Drelich, 2018; Drelich and Bowen, 2015; Ducker et al., 1994; Gao et al., 2014, 2017; Guven and Celik, 2016; Guven et al., 2015; Guven et al., 2016; Hassas et al., 2016; Moreno-Atanasio, 2013; Nguyen and Evans, 2004; Nikolaev, 2016; Pineres and Barraza, 2011; Xia, 2017; Xing et al., 2017; Yin et al., 2018; Yoon and Mao, 1996). A total of seven hypothetical heterogeneity cases were employed in the numerical experiments. The first case is a chemically homogenous particle having SR, the second case is a physically smooth particle having surface CH, the third case is a physically smooth particle having surface CAH, the fourth case is a particle with SR and surface CH, the fifth case is a particle with SR and surface CAH, the sixth case is a physically smooth particle having both surface CH and surface CAH, and the seventh case is a particle with SR, surface CH and surface CAH. The numerical experimental parameters for each case are presented in Table 1 and an illustration of each case is presented in Fig. 2.

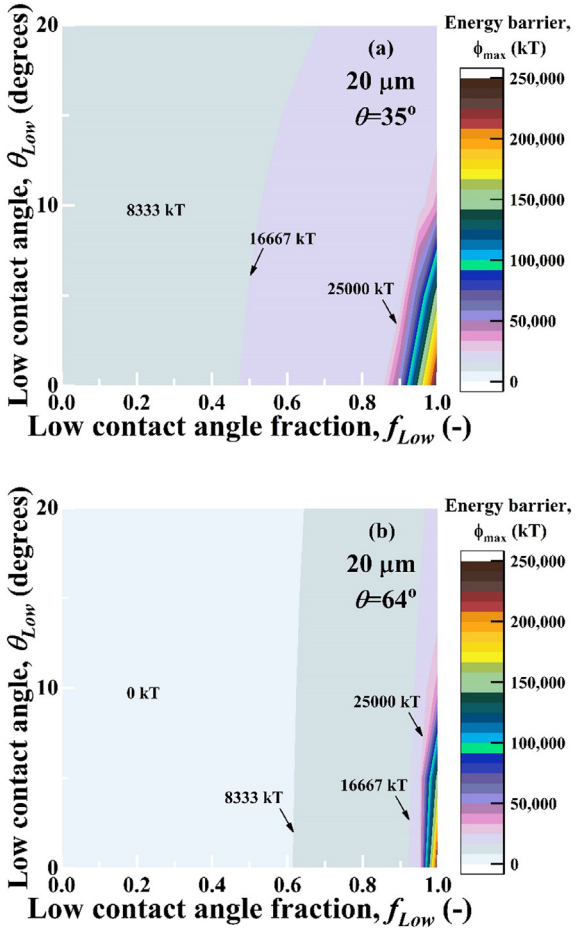

Fig. 5. Case 3: Contour plots of the XDLVO energy barrier for particle–bubble interaction as a function of θ_{Low} and its fraction for $\theta =$ (a) 35 degrees and (b) 64 degrees. Other conditions are $d_b = 1$ mm, $\xi_p = -60.75$ mV, $\xi_b = -32.78$ mV, IS = 1 mM, $\kappa^{-1} = 9.63$ nm.

3. Results and discussion

Information such as $\Phi_{\max}$ and secondary minima ($\Phi_{2\min}$) were obtained from the numerical experiments. Results not presented in this work indicate that the $\Phi_{2\min}$ is deep because of the strong HYPB interaction, suggesting the possibility of "non–contact" interaction between the particle and bubble. However, direct contact of the particle with the bubble is extremely important in an agitated flotation cell. Direct contact occurs when the particle overcomes $\Phi_{\max}$ and strong capillary forces stabilize the rising of the particle and bubble together. We therefore focus on the value of $\Phi_{\max}$ to predict attachment of the particle to the bubble in this work. Figure S1 of the Supplementary Information (SI) presents the XDLVO profile for a smooth homogeneous particle interacting with a bubble for comparison with the heterogeneity cases presented in the following sections.

3.1. Roles of single heterogeneities

Contour plots of the $\Phi_{\max}$ for case 1 are presented in Fig. 3 as a function of f_{SR} and h_{SR}. It has to be pointed out that in case 1, including all the other cases, the relatively low IS produces strong electric repulsions between the particle and bubble. One option to reduce the electric repulsion is to increase the concentration of salts to improve the flotation (Choi et al., 2016). SR offers an alternative way to improve flotation (Drelich, 2018; Drelich and Bowen, 2015; Guven et al., 2015) without increasing the IS. For example, Fig. 3 indicates a relatively low f_{SR} and h_{SR} of a few hundreds of nanometers is capable of greatly reducing the $\Phi_{\max}$, even when there is presence of strong electrostatic repulsion. For a given d_p and h_{SR}, the value of $\Phi_{\max}$ decreases from a maximum when $f_{SR} = 1$ to a minimum when f_{SR} decreases to low values. Although the cited literature (Drelich, 2018) reported the same trend for f_{SR} ($d_p = 150$ μm, h_{SR} of 5 nm), it did not provide a possible explanation based on XDLVO theory and only concluded that low f_{SR} appears to reduce the XDLVO interactions more than high f_{SR}. In our work, we explain the trends regarding f_{SR} and h_{SR} in the following discussion.

The contribution of the roughness top surface to the interaction energy in Eqs. (2)–(4) increases with f_{SR}, whereas that of the underlying smooth surface increases with $(1 - f_{SR})$. Consequently, the roughness top surface controls the interaction energy at high f_{SR}, whereas as the underlying smooth surface is more important for small f_{SR}. The value of $\Phi_{\max}$ decreases with decreasing f_{SR} because the interaction from the underlying surface becomes more important and this interaction occurs at a larger separation of $H + h_{SR}$ (Fig. 1). Conversely, $\Phi_{\max}$ increases with f_{SR} because the interaction from the roughness top dominates and this interaction occurs at a shorter separation of H. Recall that the interaction energy increases in magnitude at shorter H. Eqs. (5)–(7) indicates that dependence of VDW, EDL and HYPB on separation distance is proportional to $-1/(6H)$, $\exp(-\kappa H)$ and $1/H$, respectively. Hence, the value of $\Phi_{\max}$ is influenced simultaneously by h_{SR} and f_{SR}. In addition, the $\Phi_{\max}$ increases as d_p increases (Fig. 3) hindering the particle – bubble interaction. It is known in mineral flotation that coarse particle sizes are poorly floated (Gaudin, 1932; Koh and Schwarz, 2006).

Contour plots of the $\Phi_{\max}$ for case 2 are presented in Fig. 4 as a function of f_{p+} and ξ_{p+}. For a given d_p, the $\Phi_{\max}$ decreases as ξ_{p+} and f_{p+} increase. Conceptually, opposite charges attract each other and thus a particle that is more positively charged, either in value or fraction, will more easily attach to a negatively charged bubble. This attractive positive–negative interaction in the EDL interaction increases as ξ_{p+} becomes more positive (the factor $\xi_{p+}\xi_b$ increases in Eq. (5)) or with increasing f_{p+} (Eq. (3)). The net charge of a particle is the average value from all local charges (charge distribution) on a surface. Salt and collector counterionic groups, including pH determining ions, can reverse the net surface charge of either negative or positive charged particles. For example, quartz is negatively charged over wide range of pH and IS but can be positively charged after adsorption of high concentrations of alkylammonium acetates (Fuerstenau, 2005; Parks, 1967). The interaction energies are proportional to d_p in Eqs. (5) – (7). An increase in d_p therefore increases the magnitude of the $\Phi_{\max}$ (Fig. 4) but does not influence the trend with ξ_{p+} and f_{p+}. Consequently, only one d_p was chosen for the remaining cases (3–7).

Contour plots of the $\Phi_{\max}$ for case 3 are presented in Fig. 5 as a function of hydrophilic parameters f_{Low} and θ_{Low}. The $\Phi_{\max}$ increases with f_{Low}. The f_{Low} can be exemplified in three situations: first, a portion of the particle surface remaining hydrophilic because collector has not been adsorbed; second, a portion of the hydrophilic gangue mineral in a partially liberated mineral particle; and third, a natural (or due to grinding) uneven oxidation in the case of a sulfide mineral. Ultimately in these situations, a fraction of the particle surface is relatively hydrophobic; e.g., $(1 - f_{Low})$. A particle with a high θ (=64 degrees) covering only 30% ($f_{Low} = 70\%$) of its surface can eliminate the $\Phi_{\max}$. Although an increase in θ can considerably decrease the $\Phi_{\max}$ (Fig. 5), its effect is diminished when f_{Low} increases. Hydrophilic particles are likely to have no attachment with hydrophobic air bubbles (Yoon and Mao, 1996). Moreover, it has been reported (Sutherland et al., 1988) that significant recovery of hydrophobic particles (e.g. copper ore of an optimum size) can occur even if the surface liberation is as small as $< 10\%$. It has also been reported that quartz with a 0.5–10% surface coverage of dodecylamine floated excellently (Sutherland and Wark, 1955). Hence, CAH, mainly due to liberation and surface coverage, can have important roles in particle–bubble attachment.

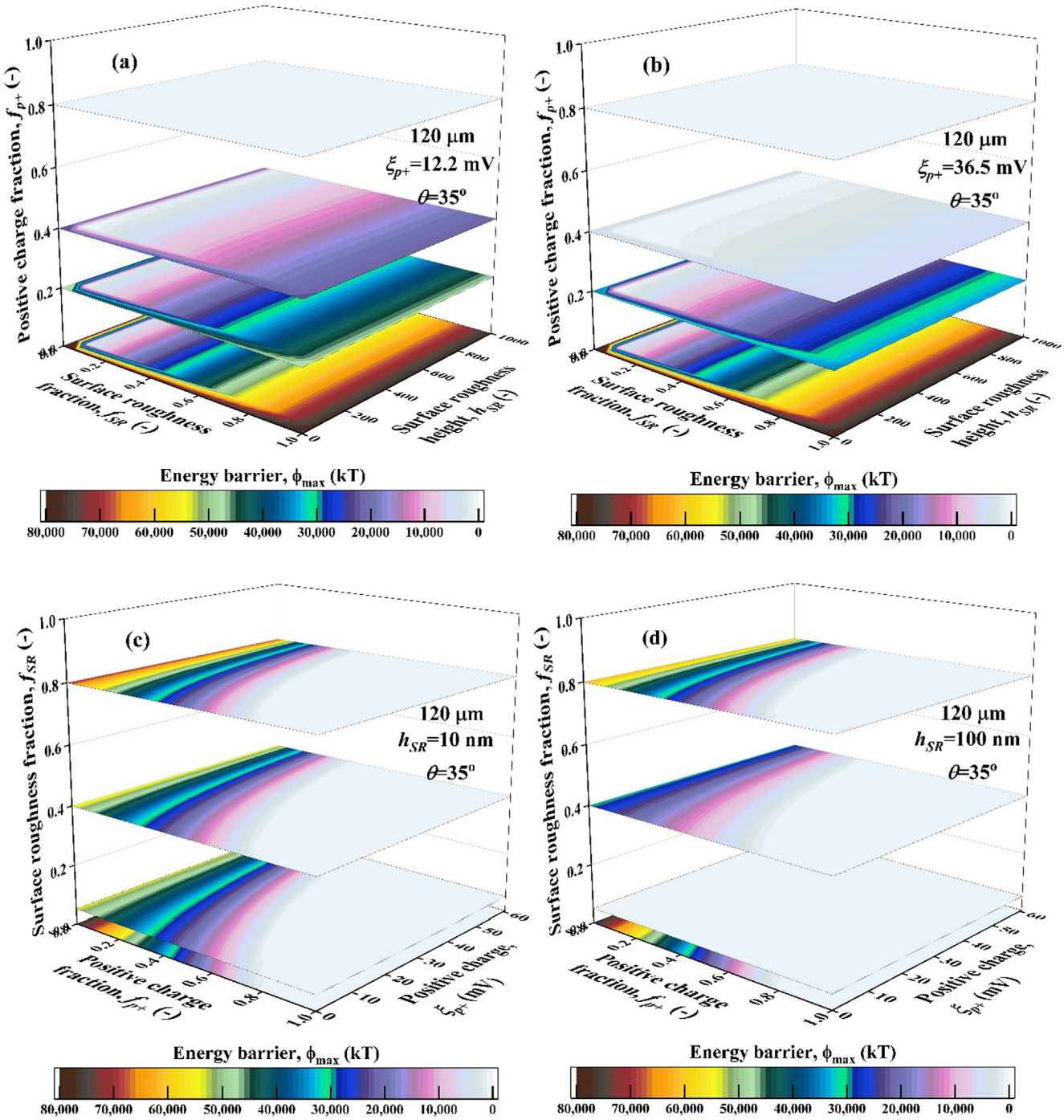

Fig. 6. Case 4: 3D surface maps of the XDLVO energy barrier for particle–bubble interaction for (a, b) SR according to CH and (c, d) CH according to SR. Other conditions are d_b = 1 mm, ξ_p = −60.75 mV, ξ_b = −32.78 mV, IS = 1 mM, κ^{-1} = 9.63 nm.

3.2. Roles of binary heterogeneities

The roles of binary heterogeneities were investigated in this section after fixing selected parameters to relatively low and high values.

Fig. 6 presents 3D surface maps of the Φ_{max} for case 4 that considered variations in both SR and CH parameters on the particle (see Table 1). The 2D slices shown in Fig. 6ab demonstrate the influence of SR parameters at different values of f_{p+} (z axis) when ξ_{p+} equals 12.2 mV (Fig. 6a) or 36.5 mV (Fig. 6b). Fig. 6a and 6b exhibit similar trends with f_{SR} and h_{SR} as shown for case 1 when f_{p+} is low (Fig. 3). However, increasing f_{p+} or ξ_{p+} produces further decreases in Φ_{max}, such that it is eliminated at higher values of f_{SR}. In fact, the effect of SR tends to disappear as the CH increases and has a dominant influence on Φ_{max}. This occurs when f_{p+} = 0.8 and ξ_{p+} = 12.2 mV in Fig. 6a, and at a lower value of f_{p+} = 0.4 when ξ_{p+} = 36.5 mV in Fig. 6b. The 2D slices shown in Fig. 6c,d demonstrate the influence of CH parameters at different values of f_{SR} (z axis) when h_{SR} equals 10 nm (Fig. 6c) or 100 nm (Fig. 6d). Fig. 6c and 6d exhibit similar trends with f_{p+} and ξ_{p+} as shown for case 2 when f_{SR} is high (Fig. 4). However, further decreases in Φ_{max} occur for small values of f_{SR}, especially when h_{SR} = 100 nm (Fig. 6d). These results indicate that CH has a dominant influence on Φ_{max} when f_{p+} and ξ_{p+} are large, but that small amounts of SR can have a controlling influence when f_{p+} and ξ_{p+} are below a threshold. Hence, a combination of low f_{SR} and high f_{p+} can reduce the Φ_{max} and promote

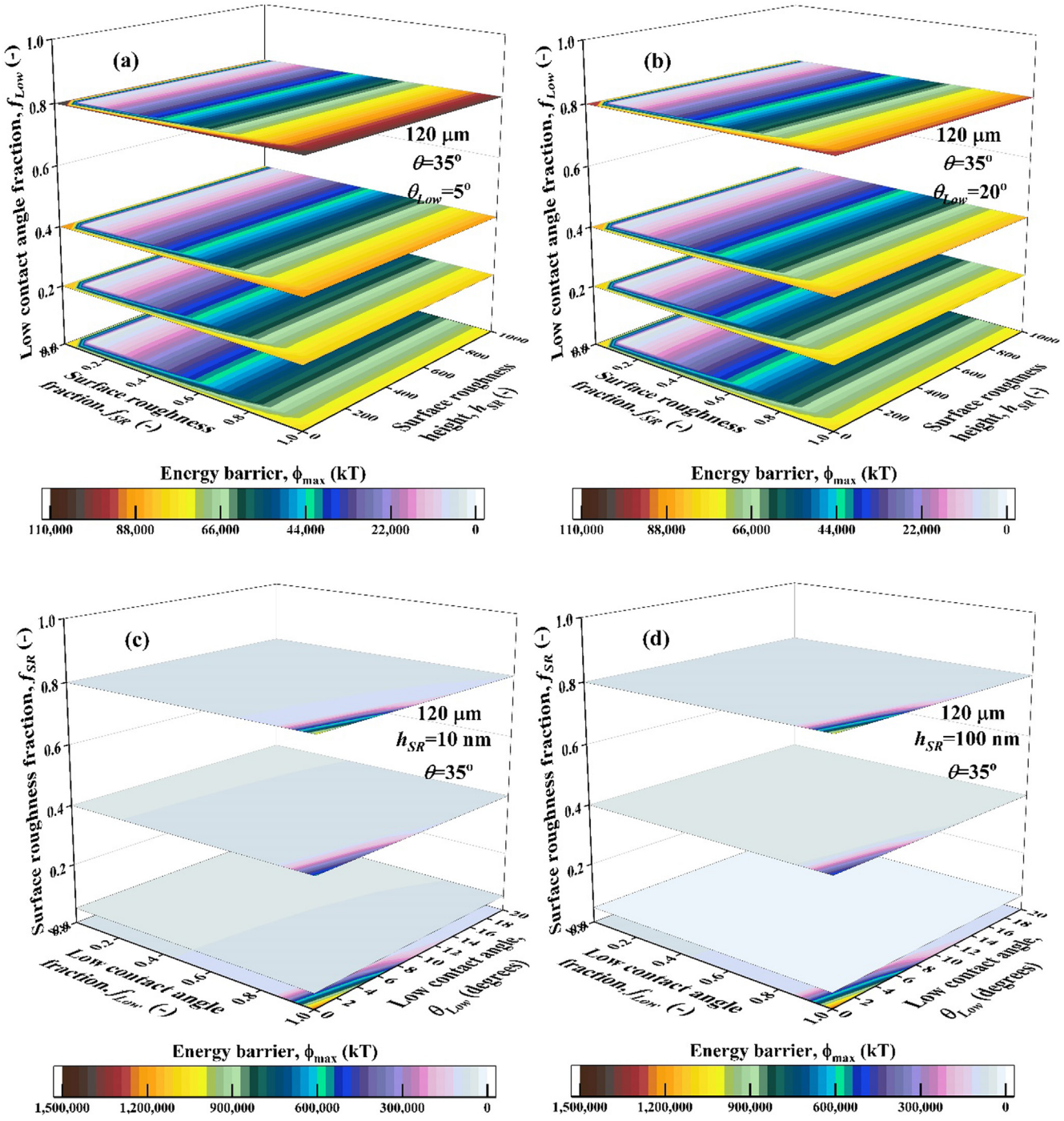

Fig. 7. Case 5: 3D surface maps of the XDLVO energy barrier for particle–bubble interaction for (a, b) SR according to CAH and (c, d) CAH according to SR. Other conditions are $d_b = 1$ mm, $\xi_p = -60.75$ mV, $\xi_b = -32.78$ mV, IS = 1 mM, $\kappa^{-1} = 9.63$ nm. Note the difference in scale.

particle–bubble interaction.

Fig. 7 presents 3D surface maps of the Φ_{max} for case 5 that considered variations in both SR and CAH parameters on the particle (see Table 1). The 2D slices shown in Fig. 7ab demonstrate the influence of SR parameters at different values of f_{Low} (z axis) when θ_{Low} equals 5 degrees (Fig. 7a) or 20 degrees (Fig. 7b). Fig. 7a and 7b exhibit similar trends with f_{SR} and h_{SR} as shown for case 1 (Fig. 3). This indicates that the effects of the SR remain large despite an increase in the CAH. However, decreasing f_{Low} produces further decreases in Φ_{max}, such that influence of SR is enhanced and roughness effects are observed at higher values of f_{SR}. Conversely, lower values of θ_{Low} increase the Φ_{max} (Fig. 4) slightly and this diminishes the influence of SR (comparison of Fig. 7a and b). The 2D slices shown in Fig. 7c,d demonstrate the influence of CAH parameters at different values of f_{SR} (z axis) when h_{SR} equals 10 nm (Fig. 7c) or 100 nm (Fig. 7d). Fig. 7c and 7d exhibit similar trends with f_{Low} and θ_{Low} as shown for case 3 when f_{SR} is high (Fig. 5). However, the value of Φ_{max} was eliminated for small values of f_{SR}. A combination of low f_{SR} and low f_{Low} can therefore reduce the Φ_{max} and promote particle–bubble interaction.

Fig. 8 presents 3D surface maps of the Φ_{max} for case 6 when CH and CAH parameters on the particle were varied (see Table 1). The 2D slices shown in Fig. 8a,b demonstrate the influence of charge heterogeneity parameters at different values of f_{Low} (z axis) when θ_{Low} equals 5 degrees (Fig. 8a) or 20 degrees (Fig. 8b). Fig. 8a and 8b exhibit similar

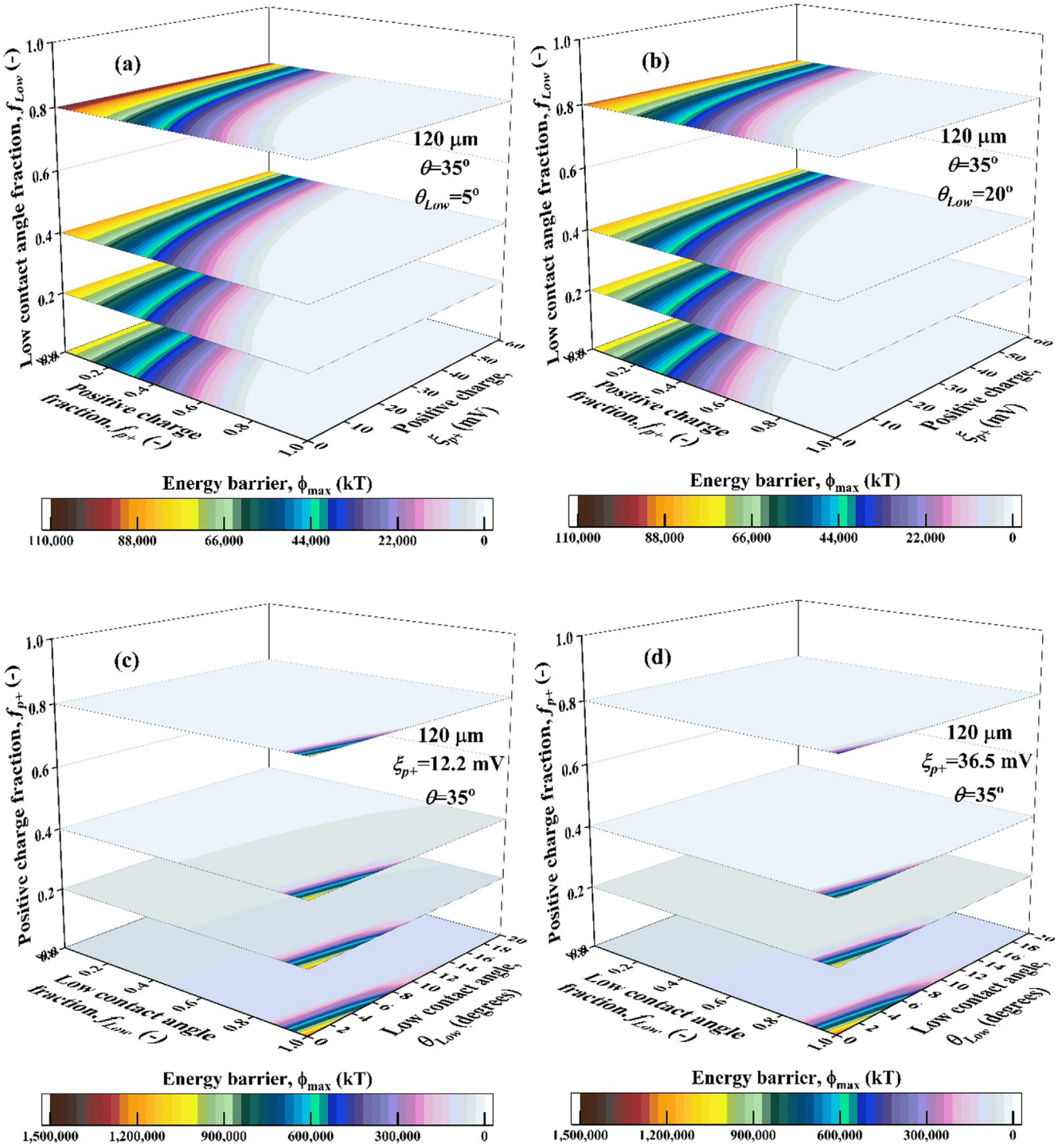

Fig. 8. Case 6: 3D surface maps of the XDLVO energy barrier for particle–bubble interaction for (a, b) CH according to CAH and (c, d) CAH according to CH. Other conditions are d_b = 1 mm, ξ_p = −60.75 mV, ξ_b = −32.78 mV, IS = 1 mM, κ^{-1} = 9.63 nm. Note the difference in scale.

trends with f_{p+} and ξ_{p+} as shown for case 2 (Fig. 4), and an increase in CAH apparently does not have a large influence on the Φ_{max}. The 2D slices shown in Fig. 8c,d demonstrate the influence of CAH parameters at different values of f_{p+} (z axis) when ξ_{p+} equals 12.2 mV (Fig. 8c) or 36.5 mV (Fig. 8d). Fig. 8c and 8d exhibit similar trends with f_{Low} and θ_{Low} as shown for case 3 when f_{p+} is low (Fig. 5). However, increasing f_{p+} strongly decreases Φ_{max} and reduces the influence of CAH. It is therefore suggested that the CH (f_{p+} and ξ_{p+}) has more impact on the Φ_{max} than the CAH (f_{Low} and θ_{Low}). A particle surface having a combination of low–medium f_{Low} and high f_{p+} will strongly influence the particle–bubble interaction.

4. Roles of ternary heterogeneities

Lastly, case 7 considers a more realistic particle surface having combined SR, CH and CAH. The value of the Φ_{max} was calculated for a total of 16,000 unique combinations of f_{SR}, f_{p+}, f_{Low}, θ, ξ_{p+}, h_{SR} and θ_{Low}. Table 1 provides details of the considered parameter ranges. The multivariable analysis in Minitab 19 (e.g., Multiple Correspondence analysis) was used to analyze this whole data set and results are shown

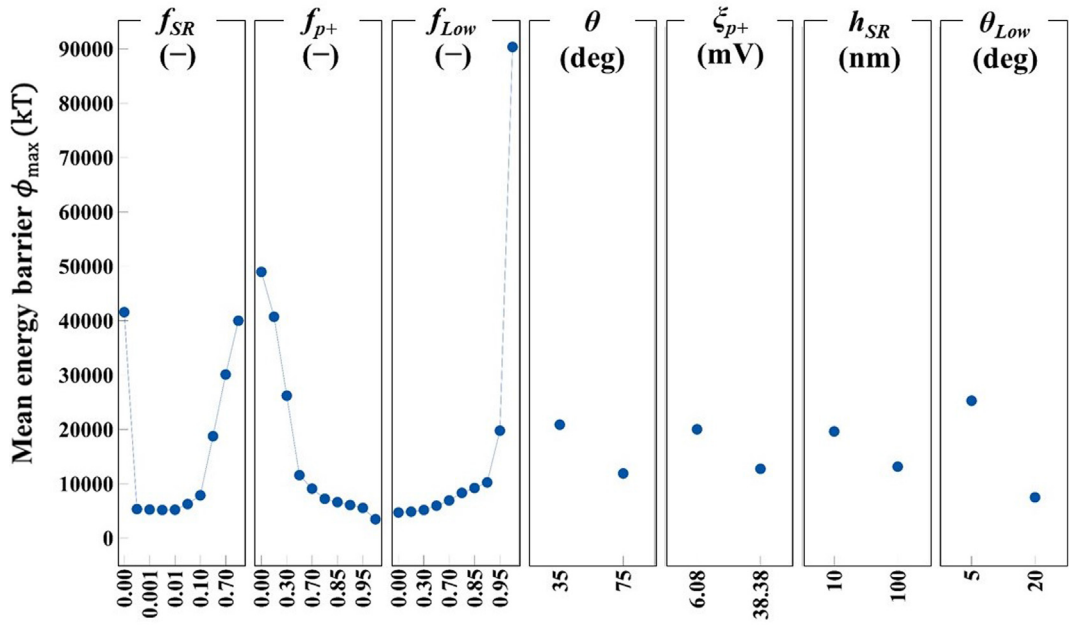

Fig. 9. Main effects plot for the variables analyzed in Case 7. d_b = 1 mm, ξ_p = −60.75 mV, ξ_b = −32.78 mV, IS = 1 mM, κ^{-1} = 9.63 nm. For each variable n = 16,000.

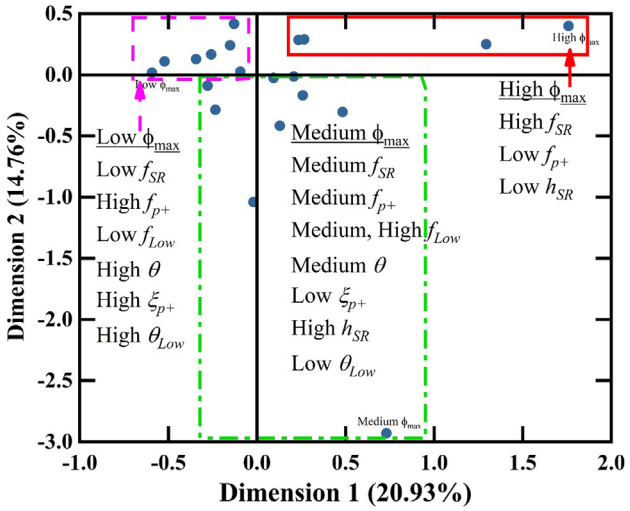

Fig. 10. Correspondence plots of Case 7 for the combined effects of SR, CH and CAH on energy barrier. d_b = 1 mm, ξ_p = −60.75 mV, ξ_b = −32.78 mV, IS = 1 mM, κ^{-1} = 9.63 nm. For each variable n = 16,000.

in Figs. 9 and 10. Fig. 9 shows the trends that the Φ_{max} has with individual variables. The f_{SR} seems to have a quadratic influence on the Φ_{max}, the f_{p+} and f_{Low} seem to have an exponential influence, and the θ, ξ_{p+}, h_{SR} and θ_{Low} seem to have a linear influence. Apparently, the Φ_{max} is influenced in the order $h_{SR} \sim \xi_{p+} \sim \theta < \theta_{Low} < f_{Low} < f_{SR} < f_{p+}$.

Table 2 presents a classification of variables and Φ_{max} into low, medium, and high ranges based on the Minitab 19 multivariable analysis. Each unique combination of variables and associated Φ_{max} were retained after the classification. A correspondence plot presented in the Fig. 10 suggests the variable combination ranges that result in low, medium, and high categories of Φ_{max}. The multiple correspondence analysis creates artificial dimensions (coordinates) to compare variances (e.g., inertia or the ratio between individual variability and the total variability). Fig. 10 shows the first two dimensions that have the highest percentage of inertia which is one measure of the quality of the results. The low category for Φ_{max} is likely to occur when f_{SR} = low, f_{p+} = high, f_{Low} = low, θ = high, ξ_{p+} = high and θ_{Low} = high. The medium category for Φ_{max} is likely to occur when f_{SR} = medium, f_{p+} = medium, f_{Low} = medium and high, θ = medium, ξ_{p+} = low, h_{SR} = high and θ_{Low} = low. Finally, the highest category for Φ_{max} is likely to occur when f_{SR} = high, f_{p+} = low and h_{SR} = low.

It should be mentioned that differences in the relative importance of SR, CH, and CAH may occur depending on selected parameter values, solution chemistries, collector type, particle sizes, phases, and whether detachment is considered. For example, the VDW interaction is attractive for particle–solid interaction, whereas it is repulsive for particle–bubble interactions. The HYPB attraction is much greater for particle–bubble systems than most particle–solid systems. Furthermore, CH

Table 2
Selected ranges of values for the variables investigated in Case 7.

Variable	Range		
	Low	Medium	High
f_{SR} (-)	0–0.01	$0.01 < f_{SR} \leq 0.2$	$0.2 < f_{SR} \leq 1$
f_{p+} (-)	0–0.2	$0.2 < f_{p+} \leq 0.6$	$0.6 < f_{p+} \leq 1$
f_{Low} (-)	0–0.2	$0.2 < f_{Low} \leq 0.6$	$0.6 < f_{Low} \leq 1$
θ (deg)	0–20	$20 < \theta \leq 50$	$50 < \theta \leq 180$
ξ_{p+} (mV)	0–10	$10 < \xi_{p+} \leq 30$	$30 < \xi_{p+} \leq 70$
h_{SR} (nm)	0–200	$200 < h_{SR} \leq 600$	$600 < h_{SR} \leq 1000$
θ_{Low} (deg)	0–5	$5 < \theta_{Low} \leq 10$	$10 < \theta_{Low} \leq 35$
Φ_{max} (kT)	$0–1\times10^3$	$1\times10^3 < \Phi_{max} \leq 1\times10^4$	$1\times10^4 < \Phi_{max} \leq 1\times10^8$

and CAH mainly influence the Φ_{max} in particle–solid interaction, whereas only low fractions of SR are known to create shallow primary minimum interactions that are susceptible to diffusive or hydrodynamic release from a particle–solid interface (Bradford et al., 2017 and 2018).

5. Conclusions

This work investigated the individual and combined effects of particle SR, CH and CAH on the Φ_{max} for particle–bubble interaction. The influence of f_{SR}, f_{p+} and f_{Low} on the Φ_{max} is quadratic, exponential, and exponential, respectively, and their apparent strength is in the order $f_{Low} < f_{SR} < f_{p+}$. The combined effect of the heterogeneity fractions are expected to result in low, medium and high ranges of Φ_{max} (see Case 7 for details on the combinations and ranges). This work focused on the physicochemical aspects that predict the attachment of a particle to a bubble and future work should also consider the stabilization of the particle after attachment, and their contribution when hydrodynamics are also considered. A final note is that even though the Φ_{max} is much higher than in typical colloidal systems (Bradford et al., 2017 and 2018), bubble and particle velocities can result in high kinetic energy during collision such that the particle can jump over the Φ_{max} if it is sufficiently small and attachment can occur. This can be seen with the following example based in previous literature (Yoon et al., 2016). Imagine a silica particle (d_p = 120 μm) and a bubble near an impeller. The particle of mass m_p approaches the bubble surface at a critical distance with a velocity vel_p of 1 cm /s and an Φ_{max} of 1000 kT (4.11×10^{-18} J) (the limit of the low Φ_{max} in Table 2). The probability of attachment is calculated as $\exp(-\Phi_{max}/E_k)$, where E_k is the particle kinetic energy calculated as $0.5 \cdot m_p \cdot vel_p$. Accordingly, the particle will have a probability of attachment of 91%. On the contrary, if the same particle is far away from the impeller its velocity is much lower, say, 0.1 cm/s, and in that situation, its probability of attachment will be 0.01%. Therefore, the effects of hydrodynamics will be considered in a future work. The validation of this work is deemed to the, currently not achieved, preparation of well–controlled SR, CH and CAH on mineral surfaces.

CRediT authorship contribution statement

Allan Gomez-Flores: Methodology, Investigation, Software, Writing - original draft. **Scott A. Bradford:** Writing - review & editing. **Gukhwa Hwang:** Writing - review & editing. **Graeme W. Heyes:** Writing - review & editing. **Hyunjung Kim:** Conceptualization, Supervision, Writing - review & editing.

Declaration of Competing Interest

The authors declare that they have no known competing financial interests or personal relationships that could have appeared to influence the work reported in this paper.

Acknowledgements

This work was supported by the National Research Foundation of Korea (NRF) grant funded by the Korea government (MSIT) (No. NRF-2020R1A2C1013851).

Appendix A. Supplementary material

Supplementary data to this article can be found online at https://doi.org/10.1016/j.mineng.2020.106472. XDLVO profile for a homogeneous particle interacting with a bubble.

References

Ahmed, M.M., 2010. Effect of comminution on particle shape and surface roughness and their relation to flotation process. Int. J. Miner. Process 94 (3–4), 180–191.
Bradford, S.A., Kim, H., Shen, C.Y., Sasidharan, S., Shang, J.Y., 2017. Contributions of Nanoscale Roughness to Anomalous Colloid Retention and Stability Behavior. Langmuir 33 (38), 10094–10105.
Bradford, S.A., Sasidharan, S., Kim, H., Hwang, G., 2018. Comparison of Types and Amounts of Nanoscale Heterogeneity on Bacteria Retention. Front. Environ. Sci. 6 (56).
Cai, L., Zhu, J.H., Hou, Y.L., Tong, M.P., Kim, H., 2015. Influence of gravity on transport and retention of representative engineered nanoparticles in quartz sand. J. Contam. Hydrol. 181, 153–160.
Chen, Y.R., Xia, W.C., Xie, G.Y., 2018. Contact angle and induction time of air bubble on flat coal surface of different roughness. Fuel 222, 35–41.
Choi, J., Choi, S.Q., Park, K., Han, Y., Kim, H., 2016. Flotation behaviour of malachite in mono- and di-valent salt solutions using sodium oleate as a collector. Int. J. Miner. Process 146, 38–45.
Drelich, J., Wang, Y.U., 2011. Charge heterogeneity of surfaces: Mapping and effects on surface forces. Adv. Colloid. Interfac. 165 (2), 91–101.
Drelich, J.W., 2018. A simplified analysis of the effect of nano-asperities on particle-bubble interactions. Physicochem. Probl. Mi. 54 (1), 10–18.
Drelich, J.W., Bowen, P.K., 2015. Hydrophobic nano-asperities in control of energy barrier during particle-surface interactions. Surf. Innov. 3 (3), 164–171.
Ducker, W.A., Xu, Z.G., Israelachvili, J.N., 1994. Measurements of Hydrophobic and DLVO Forces in Bubble-Surface Interactions in Aqueous-Solutions. Langmuir 10 (9), 3279–3289.
Falconer, J.L., Grainger, D.W., 2018. In vivo comparisons of silver nanoparticle and silver ion transport after intranasal delivery in mice. J. Control Release 269, 1–9.
Fuerstenau, D.W., 2005. Pradip, Zeta potentials in the flotation of oxide and silicate minerals. Adv. Colloid Interfac. 114, 9–26.
Gao, Y., Evans, G.M., Wanless, E.J., Moreno-Atanasio, R., 2014. DEM simulation of single bubble flotation: Implications for the hydrophobic force in particle-bubble interactions. Adv. Powder Technol. 25 (4), 1177–1184.
Gao, Y., Evans, G.M., Wanless, E.J., Moreno-Atanasio, R., 2017. DEM modelling of particle-bubble capture through extended DLVO theory. Colloid Surf. A 529, 876–885.
Gaudin, A.M., 1932. Flotation, first ed. McGraw-Hill Book Company, inc., New York, London.
Gupta, A.K., Gupta, M., 2005. Synthesis and surface engineering of iron oxide nanoparticles for biomedical applications. Biomaterials 26 (18), 3995–4021.
Guven, O., Celik, M.S., 2016. Interplay of Particle Shape and Surface Roughness to Reach Maximum Flotation Efficiencies Depending on Collector Concentration. Min. Proc. Ext. Met. Rev. 37 (6), 412–417.
Guven, O., Celik, M.S., Drelich, J.W., 2015. Flotation of methylated roughened glass particles and analysis of particle-bubble energy barrier. Miner. Eng. 79, 125–132.
Guven, O., Karakas, F., Kodrazi, N., Celik, M.S., 2016. Dependence of morphology on anionic flotation of alumina. Int. J. Miner. Process 156, 69–74.
Han, Y., Hwang, G., Kim, D., Bradford, S.A., Lee, B., Eom, I., Kim, P.J., Choi, S.Q., Kim, H., 2016. Transport, retention, and long-term release behavior of ZnO nanoparticle aggregates in saturated quartz sand: Role of solution pH and biofilm coating. Water Res. 90, 247–257.
Hassas, B.V., Caliskan, H., Guven, O., Karakas, F., Cinar, M., Celik, M.S., 2016. Effect of roughness and shape factor on flotation characteristics of glass beads. Colloid Surf. A 492, 88–99.
Hogg, R., Healy, T.W., Fuerstenau, D.W., 1966. Mutual Coagulation of Colloidal Dispersions. T Faraday Soc. 62 (522p), 1638-+.
Israelachvili, J.N., 2011. Intermolecular and surface forces, 3rd ed. Academic Press, Burlington Mass.
Israelachvili, J.N., Pashley, R.M., 1984. Measurement of the Hydrophobic Interaction between 2 Hydrophobic Surfaces in Aqueous-Electrolyte Solutions. J. Colloid Interf. Sci. 98 (2), 500–514.
Kim, G., Choi, J., Silva, R.A., Song, Y., Kim, H., 2017. Feasibility of bench-scale selective bioflotation of copper oxide minerals using Rhodococcus opacus. Hydrometallurgy 168, 94–102.
Koh, P.T.L., Schwarz, M.P., 2006. CFD modelling of bubble-particle attachments in flotation cells. Miner. Eng. 19 (6–8), 619–626.
Kulkarni, R.D., Somasundaran, P., 1976. Mineralogical Heterogeneity of Ore Particles and Its Effects on Their Interfacial Characteristics. Powder Technol. 14 (2), 279–285.
Medout-Marere, V., El Ghzaoui, A., Charnay, C., Douillard, J.M., Chauveteau, G., Partyka, S., 2000. Surface heterogeneity of passively oxidized silicon carbide particles: Hydrophobic-hydrophilic partition. J. Colloid Interf.. Sci. 223 (2), 205–214.
Moreno-Atanasio, R., 2013. Influence of the hydrophobic force model on the capture of particles by bubbles: A computational study using Discrete Element Method. Adv. Powder Technol. 24 (4), 786–795.
Nguyen, A.V., Evans, G.M., 2004. Attachment interaction between air bubbles and particles in froth flotation. Exp. Therm. Fluid Sci. 28 (5), 381–385.
Nikolaev, A., 2016. Flotation kinetic model with respect to particle heterogeneity and roughness. Int. J. Miner. Process 155, 74–82.
Park, K., Choi, J., Gomez-Flores, A., Kim, H., 2015. Flotation Behavior of Arsenopyrite and Pyrite, and Their Selective Separation. Mater. Trans. 56 (3), 435–440.
Parks, G.A., 1967. Aqueous Surface Chemistry of Oxides and Complex Oxide Minerals. Adv. Chem.. Ser. 67 121-+.
Peng, S.N., Wu, D., Ge, Z., Tong, M.P., Kim, H.J., 2017. Influence of graphene oxide on the transport and deposition behaviors of colloids in saturated porous media. Environ Pollut 225, 141–149.

Pineres, J., Barraza, J., 2011. Energy barrier of aggregates coal particle-bubble through the extended DLVO theory. Int. J. Miner. Process 100 (1–2), 14–20.
Ralston, J., 2020. The scientific legacy of Joseph Kitchener- its impact in colloid science and flotation. Miner. Eng. 149, 106230.
Silva, R.A., Park, J., Hong, J., Kim, H.J., Park, J., Kim, H., 2015a. Natural organic matter affects the treatment of mine tailings through bioleaching processes. Adv. Mater. Res. 1130, 656–659.
Silva, R.A., Park, J., Lee, E., Park, J., Choi, S.Q., Kim, H., 2015b. Influence of bacterial adhesion on copper extraction from printed circuit boards. Sep. Purif. Technol. 143, 169–176.
Song, L.F., Elimelech, M., 1994. Transient Deposition of Colloidal Particles in Heterogeneous Porous-Media. J. Colloid Interf. Sci. 167 (2), 301–313.
Sutherland, D.N., Gottlieb, P., Heyes, G.W., Jackson, B.R., 1988. The influence of mineral locking on flotation behaviour. In: In Proc. XVI International Mineral Processing Congress, Stockholm, Sweden, pp. 535–545.
Sutherland, K.L., Wark, I.W., 1955. Principles of flotation. Rev and enl. edn. Australasian Institute of Mining and Metallurgy, Melbourne.
Van Oss, C.J., 1994. Interfacial forces in aqueous media. M. Dekker, New York.
Vanoss, C.J., 1993. Acid-Base Interfacial Interactions in Aqueous-Media. Colloid Surf. A 78, 1–49.
Xia, W.C., 2017. Role of surface roughness in the attachment time between air bubble and flat ultra-low-ash coal surface. Int. J. Miner Process 168, 19–24.
Xie, L., Wang, J.Y., Shi, C., Cui, X., Huang, J., Zhang, H., Liu, Q., Liu, Q.X., Zeng, H.B., 2017. Mapping the Nanoscale Heterogeneity of Surface Hydrophobicity on the Sphalerite Mineral. J. Phys. Chem. C 121 (10), 5620–5628.
Xing, Y.W., Gui, X.H., Karakas, F., Cao, Y.J., 2017. Role of Collectors and Depressants in Mineral Flotation: A Theoretical Analysis Based on Extended DLVO Theory. Min.-Basel 7 (11).
Yin, W., Zhu, Z., Yang, B., Fu, Y., Yao, J., 2018. Contribution of particle shape and surface roughness on the flotation behavior of low-ash coking coal. Energy Sources. Part A: Recovery Utilizat. Environ. Effects 41 (5), 636–644.
Yoon, R.H., Mao, L.Q., 1996. Application of extended DLVO theory.4. Derivation of flotation rate equation from first principles. J. Colloid Interf. Sci. 181 (2), 613–626.
Yoon, R.H., Soni, G., Huang, K.W., Park, S., Pan, L., 2016. Development of a turbulent flotation model from first principles and its validation. Int. J. Miner. Process 156, 43–51.
Zhang, M., Bradford, S.A., Simunek, J., Vereecken, H., Klumpp, E., 2016. Do Goethite Surfaces Really Control the Transport and Retention of Multi-Walled Carbon Nanotubes in Chemically Heterogeneous Porous Media? Environ. Sci. Technol. 50 (23), 12713–12721.